AGU PUBLICATIONS

JGR

Journal of Geophysical Research: Solid Earth

RESEARCH ARTICLE
10.1002/2013JB010308

Key Points:
- Vertical slips across fault deduced from the horizontal slips
- LF as a fold scarp formed over an active axial hinge zone
- Most surface deformation localized within active axial hinges

Supporting Information:
- Photos locations and meta-information.
- The profiles locations.

Correspondence to:
Y.-G. Chen,
ygchen@ntu.edu.tw

Citation:
Kuo, Y.-T., F. Ayoub, S. Leprince, Y.-G. Chen, J.-P. Avouac, J. B. H. Shyu, K.-Y. Lai, and Y.-J. Kuo (2014), Coseismic thrusting and folding in the 1999 M_w 7.6 Chi-Chi earthquake: A high-resolution approach by aerial photos taken from Tsaotun, central Taiwan, *J. Geophys. Res. Solid Earth*, *119*, 645–660, doi:10.1002/2013JB010308.

Received 3 JUN 2013
Accepted 5 DEC 2013
Accepted article online 17 DEC 2013
Published online 23 JAN 2014

Coseismic thrusting and folding in the 1999 M_w 7.6 Chi-Chi earthquake: A high-resolution approach by aerial photos taken from Tsaotun, central Taiwan

Yu-Ting Kuo[1], Francois Ayoub[2], Sébastien Leprince[2], Yue-Gau Chen[1], Jean-Philippe Avouac[2], J. Bruce H. Shyu[1], Kuang-Yin Lai[1], and Yu-Ju Kuo[3]

[1]Department of Geosciences, National Taiwan University, Taipei, Taiwan, [2]Division of Geological and Planetary Sciences, Caltech, Pasadena, California, USA, [3]Mathematics Department, Indiana University of Pennsylvania, Indiana, Pennsylvania, USA

Abstract We used aerial photos taken before and after the 21 September 1999, M_w 7.6, Chi-Chi earthquake in central Taiwan to measure the near-field ground deformation. A total of 12 pairs of images were processed with Co-registration of Optically Sensed Images and Correlation to produce a horizontal displacement map of a 10 km × 10 km area near Tsaotun. Using pairs of images with different viewing angles, both the horizontal and vertical slip across the fault zone can be measured. Our measurements when resampled into lower resolution are consistent with lower resolution measurements of horizontal displacements obtained from SPOT images, as well as with vertical displacements obtained from repeated leveling measurements and field observations. Horizontal strain is strongly localized along the Chelungpu fault (CLPF) and along a secondary scarp that runs parallel to the CLPF about 2 km to the east, the Ailiao fold scarp (ALF). This pattern closely matches the surface ruptures mapped in the field. Horizontal strain across CLPF correlates remarkably well with the topographic features produced by long-term deformation. The cumulative horizontal shortening across the CLPF and ALF amounts to 4.9 ± 0.4 and 6.1 ± 0.6 m, respectively, and fault-parallel displacement is 3.4 ± 0.4 m. The pattern of surface strain is consistent with the interpretation of the ALF as a fold scarp formed over an active axial hinge zone. This study shows that, even in this compressional setting, most surface deformation is localized within narrow fault zones or active axial hinges.

1. Introduction

1.1. Geological Background of Chi-Chi Earthquake

The island of Taiwan is located at the active collision boundary between the Eurasian and the Philippine Sea Plates (Figure 1). Because of this unique tectonic setting, Taiwan is characterized by dense and frequent earthquakes and many active geological structures (Figure 1). According to Global Positioning System (GPS) measures, these active structures absorb up to 80 mm/yr of convergence across the island [*Yu et al*., 1997] (Figure 1). In western Taiwan, thrust faults are the most typical active faults; in particular, the Chelungpu and the Changhua faults each absorb about half of the −35 mm/yr convergence across the foothills [*Simoes et al*., 2007] (Figure 1). These thrust faults have generated disastrous shallow earthquakes in Taiwan's short recorded history [*Wu*, 1978], the 1999 Chi-Chi earthquake being the latest among such events. This earthquake ruptured the Chelungpu fault (CLPF) [*Wu*, 1978] over a distance of about 90 km, producing a combination of thrusting and left-lateral slip consistent with the oblique convergence across the western foothills [*Chen et al*., 2001]. The focal mechanism of the earthquake indicates reverse faulting along a 29° east dipping plane with a slight sinisterly strike-slip component [*Kikuchi et al*., 2000; *Ma et al*., 2000], which was consistent with the ramp geometry of the CLPF [*Johnson et al*., 2001]. Coseismic ground displacements along the surface ruptures showed mostly reverse slip, but there was also evidence of significant left-lateral slip, especially along the southern part of the rupture [e.g., *Chen et al*., 2001].

1.2. Why Mapping the Ground Surface Deformation?

Understanding the distributed surface deformation as a result of earthquakes is an important subject to further study on either the practical issue of seismic hazard mitigation or as a scientific one of fault kinematics. It is apparent, revealed by past seismic events, that damages to buildings can result not only from

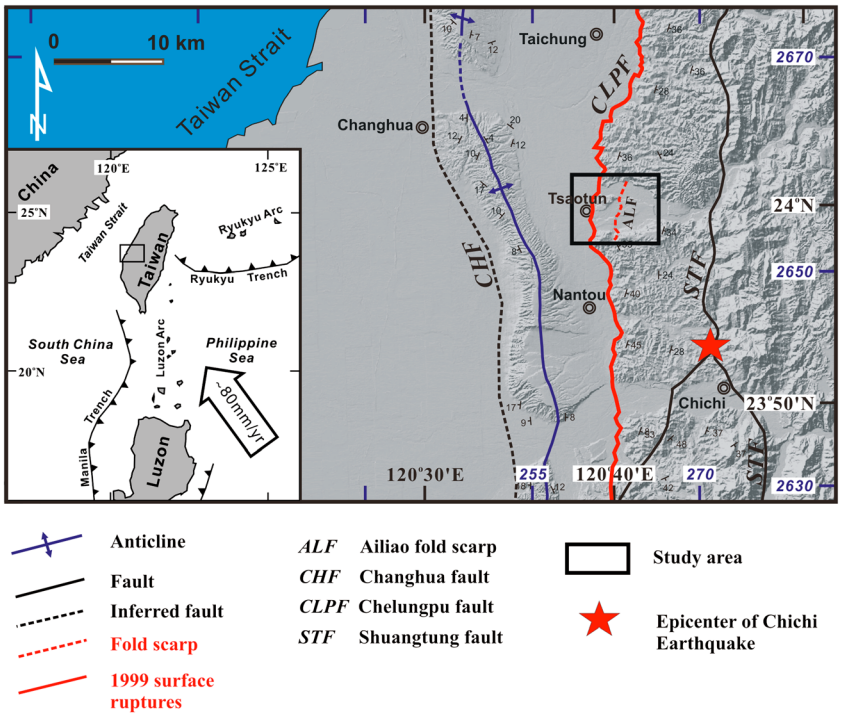

Figure 1. Topography map of western central Taiwan indicating the epicenter and surface ruptures of Chi-Chi earthquake [after *Chen et al*., 2002]. The solid red line indicates the Chi-Chi earthquake surface rupture along the Chelungpu fault as mapped in the field [*CGS*, 1999]. The dashed red line shows the location of a coseismically formed scarp [*CGS*, 1999], interpreted as a fold scarp [*Chen et al*., 2007a], called the Ailiao fold scarp. The box indicates the area within which surface displacements were measured using the correlation of aerial photos. The coordinate system is combined by geographic coordinates and universal transverse Mercator (UTM)-51N.

ground shaking but also from local static ground strain. A significant percentage of the damage caused by the disastrous 1999, M_w 7.6, Chi-Chi earthquake (central western Taiwan) closely follows the areas with concentrated surface strain, that is, surface ruptures along the CLPF [*Central Geological Survey* (*CGS*), 1999] (Figures 1 and 2). Therefore, to learn why and how the ground strain is distributed is no doubt a stepping stone for seismic hazard prevention in future events. Information about active faults and their past seismic activity mostly comes from the interpretation of their morphologic signatures or shallow expressions observed in trenches. It is possible, however, that a zone with significant anelastic deformation may be actually wide, as observed in a few places where anthropogenic structures with known preseismic geometry were surveyed [*McGill and Rubin*, 1999; *Rockwell et al*., 2002]. Studies on past seismic activity or determination of fault slip rate from offset geomorphic features in sporadically distributed sites may be biased or incomplete. Moreover, in a compressional setting, where thrusting is generally associated with folding, a significant percentage of the deformation would be sometimes broadly distributed regardless of the thrust fault tips reaching the surface or not [e.g., *Avouac et al*., 1993; *Roering et al*., 1997; *Dolan and Avouac*, 2007], as is the case for the CLPF found in 1999 Chi-Chi, Taiwan, earthquake. This has been well observed and documented at decametric trenches [e.g., *Lee et al*., 2001; *Streig et al*., 2007].

1.3. How to Map the Ground Surface Deformation?

To learn the distributed ground deformation, optical images have been approved as usable data source, especially appropriate in coseismic ground deformation when using the technique of subpixel correlation to compare the paired images taken before and after the earthquake [e.g., *Van Puymbroeck et al*., 2000; *Michel and Avouac*, 2002; *Klinger et al*., 2006; *Michel and Avouac*, 2006]. However, the displacement is detectable only if it is larger than one tenth of the image resolution [e.g., *Leprince et al*., 2007]. Therefore, it is adequate to study the coseismic displacement because the ground displacement produced by a large earthquake is usually more than the detecting limit mentioned above. It is worthy to note that this tool can obtain distributed ground displacements and map relevant values covering the whole imagery. On the other hand, the Differential Interferometry Synthetic Aperture Radar (D-InSAR) technique also can be utilized as another data

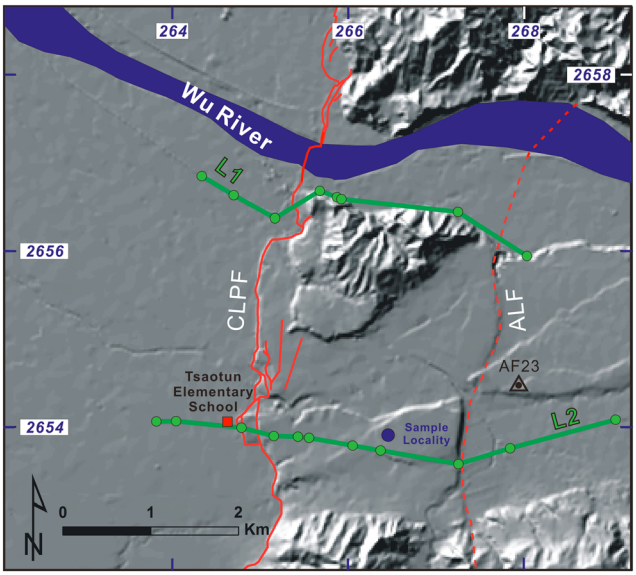

Figure 2. The cartographic coordinate system is UTM-51N. The shaded topography of the Tsaotun area was used in this study (Aerial Survey Office, Forestry Bureau, Taiwan). The Chelungpu fault (CLPF) [*CGS*, 1999] is shown as a continuous red line and the Ailiao fold scarp (ALF) [*CGS*, 1999; *Chen et al*., 2007a] is shown as the dashed red line. Locations L1 and L2 show the locations of the leveling lines of Figure 6. There is only one coseismic Global Positioning System (GPS) data (AF23) in Tsaotun area, and the location is shown in black triangle [*Yu et al*., 2001]. The blue circle is the location of dating sample [*Chen et al*., 2003].

source to obtain the ground deformation and its accuracy can reach centimeter grade [*Gabriel et al*., 1989; *Massonnet et al*., 1993; *Zebker et al*., 1994; *Murakami et al*., 1996]. Unfortunately, if the ground displacement is higher than half of the SAR wavelength, it no longer produces a good fringe to measure the ground deformation [*Massonnet and Rabaute*, 1993; *Massonnet and Feigl*, 1998]. It is hence impossible to apply it for the coseismic ground displacements of a large earthquake that generally produces ground displacements up to a few meters. For the case of 1999 Chi-Chi earthquake, GPS observations have already documented the total horizontal offsets of 2.4–10.1 m across the CLPF [*Yu et al*., 2001]. This is the reason why so far there is no published D-InSAR result for the hanging wall but results published for the footwall and after slip for the event of 1999. The only hanging wall displacement mapping is in the article published by Dominguez et al. in 2003, who utilized the optical satellite images (SPOT) via the subpixel correlation. These measurements showed 4–5 m of E-W convergence along the ground fault trace (thrust component) and 5–6 m of left-lateral slip. The resulted maximum slip (Taichung area) exceeded 12 m with 8 m each for horizontal fault-perpendicular and left-lateral slip, respectively. Other independent studies such as inversion of the geodetic data, SPOT measurements, and seismological data all agree with this coseismic maximum slip [e.g., *Ji et al*., 2001; *Dominguez et al*., 2003; *Loevenbruck et al*., 2004; *Hsu et al*., 2009]. Nevertheless, because of the low resolution of the source SPOT images, which is about every 10 m a pixel, the deformation signal can only be determined by looking at a sliding window of pixels and by removing noises, and therefore, Dominquez obtained a 1 km grid spacing of the deformation value [*Dominguez et al*., 2003]. This is not enough to resolve the detailed question and problem that we encountered on hazard mitigation and local fault kinematics. If we want to focus on 1–2 km length to identify the subsurface geometry, one value per 100–200 m is needed. A higher resolution of the image such as an aerial photo (1 pixel = 60 cm) could be a good source to perform this analysis.

1.4. Objectives of This Study

This study therefore aims at publishing a high-resolution map of the horizontal coseismic deformation caused by the Chi-Chi earthquake in the Tsaotun area, where a relatively complex pattern of ruptures with scarps several meters high have been reported [*CGS*, 1999]. This area has been also found with a subsidiary surface rupture-like deformation in addition to the main thrust, the CLPF. This is a reactivated scarp that had been mapped as an active fault, the Ailiao fault [*Yang*, 1986] because of its geomorphological expression, which lies about 2 km east the CLPF surface trace. Later studies have given fundamental insights to how

earthquakes contribute to such a complicated dual-fault system [*Chen et al*., 2001, 2007b]. Along the CLPF, the fault scarp was coseismically reactivated and thrown westward during the earthquake. On the other hand, the east facing secondary scarp was displaced with a behavior of a kink fold. The correlation window of 16 × 16, 32 × 32, or 64 × 64 pixels were used in a previous pixel comparison study on panchromatic SPOT images (pixel size of 10 m) [*Dominguez et al*., 2003]. After filtering and removing noises, a deformation value was obtained for every 1 km [*Dominguez et al*., 2003]; thus, the result did not allow us to recognize the subkilometric details of interest in this area especially in the difference between CLPF and Ailiao fold scarp (ALF). In Taiwan, the resolution of aerial photos is as high as every 0.6 m a pixel. If the correlation window used in the comparison is as large as 256 × 256 pixels, the anticipated result could still reach a resolution as high as 153.6 m, a datum for the spatial ground deformation map. This advantage of such a high resolution would allow us to look at the coseismic deformation-related fault kinematics in a scale that has never been reached before. In addition, the technical innovation is also a challenge. Although the aerial photos have been used as data source before, they have been used for strike-slip predominant fault. This is the first time that this technique is being applied on a thrust fault system. It is expected to implement a new workable procedure flow to efficiently study similar events occurring in the future.

2. Methodology

2.1. Advantage of Subpixel Correlation on Aerial Photos

The subpixel correlation of optical images has been successfully applied in a number of studies when measuring horizontal coseismic ground deformation from satellite images [e.g., *Van Puymbroeck et al*., 2000; *Michel and Avouac*, 2002; *Klinger et al*., 2006] and aerial photos [*Michel and Avouac*, 2006]. The increasing number of optical imaging programs, the availability of archived data, and the better spatial resolution that can be achieved with aerial photos and recent satellite systems make the subpixel correlation of optical imagery even more attractive. This approach applied the same technique on aerial photos with an attempt to yield a high-resolution and distributed map of horizontal ground displacement that might be too distributed to be detected or measured by field survey. This technique particularly allows the distributed measurement of fault-perpendicular displacement, which can only be sporadically measured in the field. The method adopted in this study has been preliminarily described in detail in *Leprince et al*. [2007]. Subsequently, the processing flow has been used for satellite images [*Michel and Avouac*, 2006; *Ayoub et al*., 2008]. The main difference in methodology between this and the previous study on aerial photos and satellite imagery lies in the acquisition of images involving a frame camera instead of a pushbroom system, which involves images with a greater field of view, and from much lower altitude. Such spatial relationship changes on optical geometry incidentally helped us discover that the disparities measured from the correlation of images taken before and after an earthquake are sensitive to not only the horizontal but also to the vertical component of the ground displacement. As described later in this article, actually overlapping pairs of aerial photos with different viewing angles enabled us to resolve the horizontal as well as the vertical components of the fault slip [*Copley et al*., 2011; *Hollingsworth et al*., 2012; *Hollingsworth et al*., 2013].

2.2. Processing the Disparities Between Preearthquake and Postearthquake Aerial Photos

The aerial photos used in this study were taken by the Aerial Survey Office, Forestry Bureau, Taiwan. Analog films were digitized using a Photogrammetric Workstation (PS-TD) by a scan resolution of 14 microns. Twelve images each for before and after the earthquake were selected. Listed in Table S1 in the supporting information are the photo specifications, flight channels, camera types, and distribution map. Digitized films may be corrupted by scanning artifacts [*Ayoub et al*., 2009], but no scan artifacts were detected from the subsequent correlations.

The method is based on the correlation of preearthquake and postearthquake images, which are first coregistered and orthorectified on the same ground grid. The orthorectification was performed based on a 40 m preearthquake digital elevation model (DEM) and 1/5000 Topo-maps, both produced by the Aerial Survey Office, Forestry Bureau, Taiwan. The internal orientation model (geometry of the camera and optical distortions correction) detailed in the camera calibration report was taken into account for all the photos. The external orientation (attitude and geographic position of the exposure station) of the preearthquake photos were calculated and optimized using ground control points (GCPs), selected on the 1/5000 Topo-maps and in the DEM. The orthorectified preearthquake images were then used as a reference to define GCPs for the

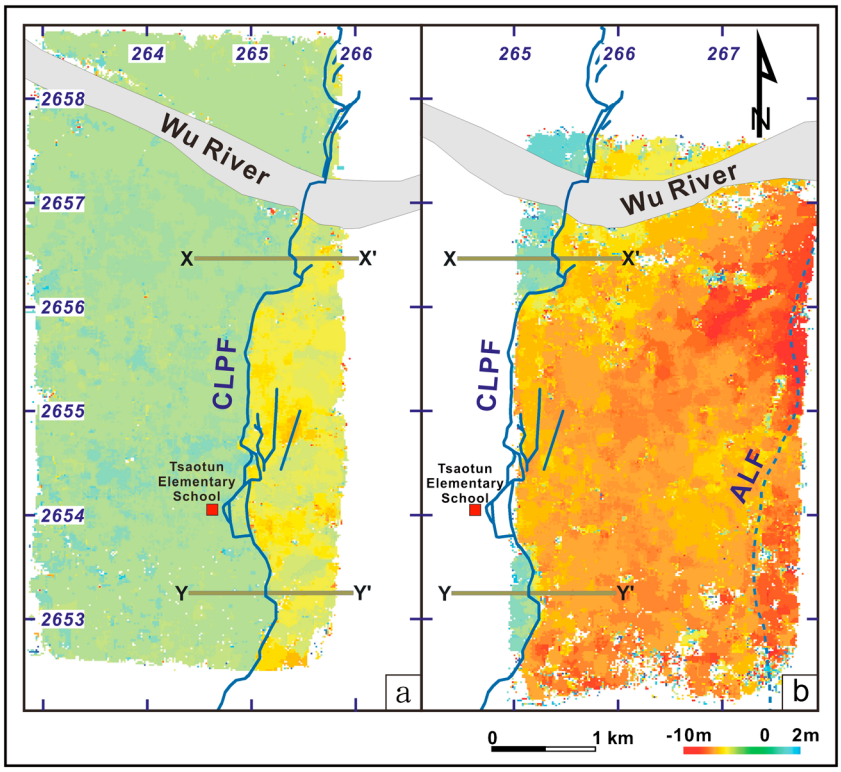

Figure 3. Mosaic of the east-west disparity maps in the Tsaotun area as measured by the correlation of two different overlapping pairs of aerial photos taken before and after the Chi-Chi earthquake. The displacements that are in the overlapping area were averaged by the measurements of the same location. (a)Western track and (b) eastern track. Cartographic coordinates are given in kilometers (UTM-51N). X-X' and Y-Y' show location of profiles of Figure 4. The continuous blue line shows the Chelungpu fault (CLPF) [*CGS*, 1999], whereas the dashed blue line indicates the location of the Ailiao fold scarp (ALF) [*CGS*, 1999; *Chen et al*., 2007a].

postearthquake photos. The ground coordinates of the postearthquake GCPs were corrected to account for the coseismic ground displacement. These corrections had been defined from the displacements measured from SPOT images [*Dominguez et al*., 2003]. The resolution of raw images is 0.6 m, and the orthorectified images were resampled by 1 m. The geometric disparities between the orthorectified preearthquake and postearthquake aerial photos were then measured and sampled on a 16 × 16 m resolution grid from correlation performed using a 128 × 128 pixels sliding window. As all procedures have been computerized, a software package, Co-registration of Optically Sensed Images and Correlation (COSI-Corr), installed under operation system ENVI has been developed for the procedure integration [*Leprince et al*., 2007]. This study takes the advantage of such a convenient tool [*Leprince et al*., 2007] to execute the image rectification, to complete the subpixel comparison, and to publish the map of ground displacements.

2.3. Uncertainties and Bias Sources

Several key sources of uncertainties or artifacts should be noted. First, the large difference between the resolution of the DEM (40 m) and the aerial photos (<1 m) may leave uncorrected parallax distortions that will be retrieved in the correlation maps as horizontal displacements. The high-frequency texture of aerial photos is susceptible to rapid decorrelation because of man-made modifications, shade orientation, changes in vegetation cover, and so on. Any area that sustained change between the two acquisition dates will decorrelate, and therefore, no displacement values could be provided. Finally, because of the coordinate system and production mode, it would be difficult to calculate the error from the different source of DEM; therefore, we chose preearthquake DEM (40 m) to process. Nevertheless, in this case, this is a thrust fault event and the hanging wall of CLPF was uplifted several meters. When we orthorectificated the postearthquake aerial photos on preearthquake DEM, we could calculate the vertical displacement, an unexpected result. It will be described in detail in the next paragraph.

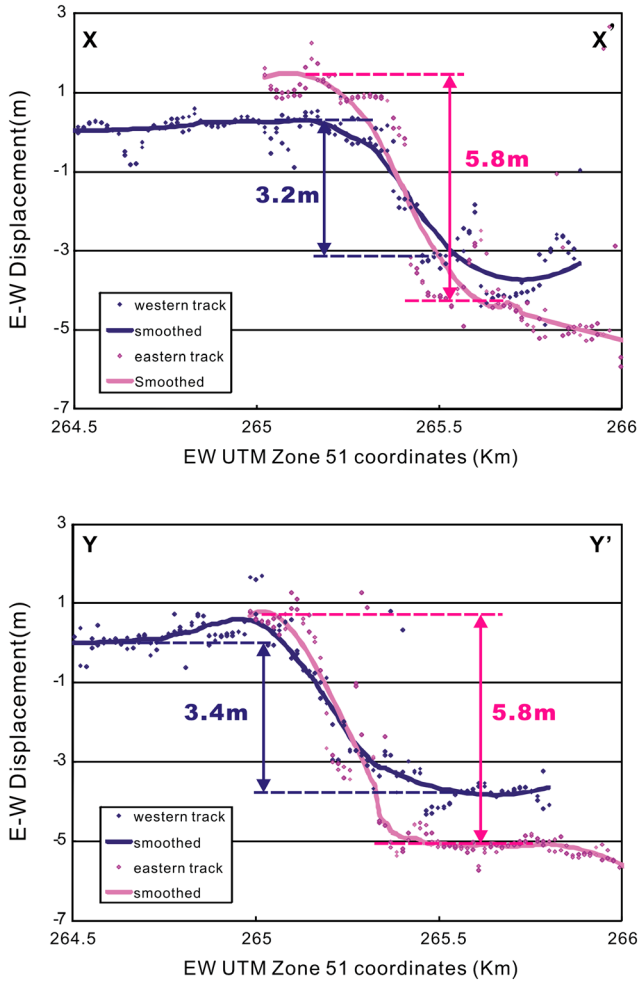

Figure 4. East-west disparities measured along the X-X′ and Y-Y′ profiles based on the correlation of the aerial photos taken along the western (pink) and eastern (blue) tracks. The locations of the X-X′ and Y-Y′ profiles are shown in Figure 3. The apparent offsets across the fault are 3.2 and 3.4 m determined from the western track and 5.8 m from the eastern track.

3. Results

3.1. The Disparity Actually Sensitive to Vertical Displacements

Figure 3 shows the E-W disparity maps measured along two different tracks covering the CLPF. The result shows a clear discontinuity along both tracks, which matches well with the surface ruptures reported by the CGS [1999]. Topographic residual is small even in the southern mountainous area, thanks to the small baseline between preearthquake and postearthquake images. However, the disparity maps computed from the two tracks show obvious differences. As seen in the profiles in Figure 4, the E-W fault offset is about 3.3 m on the western track and about 5.8 m on the eastern track. This discrepancy is the result of a vertical ground displacement seen from two different angles but using only a preearthquake DEM as illustrated by Figure 5. Trigonometric equations relate the vertical and the horizontal displacements (Figure 5). Along the X-X′ profile in Figure 2 and following Figure 5, á and â are both about 72°, then xL and xR are 3.2 m and 5.8 m, respectively. Along the Y-Y′ profile and following Figure 5, á and â are both about 71°, then xL and xR are 3.4 m and 5.8 m, respectively. Using the trigonometric relationships in Figure 5, the change of elevation can be estimated to be approximately 4.0 m along X-X′, and about 3.5 m along Y-Y′. These are only crude estimates, but they compare well with the elevation change measured along two nearby leveling profiles, L1 and L2 [*CGS*, 1999] (Figures 2 and 6). These leveling results indicate that the CLPF hanging wall was uplifted by about 3 to 4 m relative to the footwall.

To estimate unbiased horizontal displacements, we lifted the ground level up by 3 m for the preearthquake DEM over the hanging wall area of the CLPF to assume a postearthquake DEM, orthorectified, and correlated

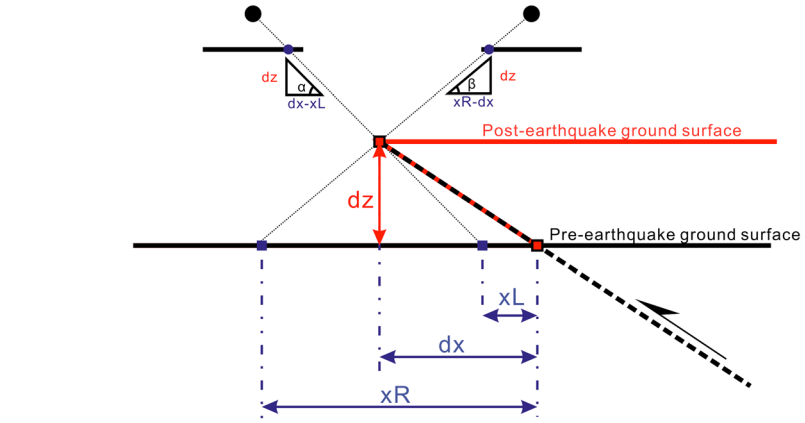

Figure 5. A simplified diagram showing how the disparities measured from the correlation aerial photos depend on coseismic horizontal (dx) and vertical (dz) displacements and on the viewing angle. For simplicity, the initial topography is assumed horizontal and the hanging wall is assumed rigid and fixed (it defines the reference frame); the footwall is assumed to be rigid and translated by a constant vector. The black line represents the ground surface before the earthquake, whereas the red line indicates the ground surface after the earthquake. We assume that all other sources of geometric distortions are negligible. "xL" is the apparent coseismic offset of the left pair, and "xR" is the apparent coseismic offset from the right pair. Because the vertical offset as a result of the earthquake is not accounted for, xL and xR are different. This difference can be used to separate dx and dz from xL and xR.

the aerial photos again. After such correction, the disparities should only reflect the horizontal displacements. The profiles running into the disparity field determined from the eastern and western pairs of images were now consistent (Figure 7). The E-W horizontal displacements across the CLPF are estimated to be 4.5 m and 4.6 m along X-X′ and Y-Y′ profiles, respectively (Figure 7). This shows the possibility of estimating vertical displacements in addition to horizontal from aerial photos acquired with different viewing angles, although the spatial resolution and accuracy of the vertical component can only be crude. In any case, estimating vertical displacements is necessary to estimate unbiased horizontal displacements if the postearthquake DEM has not been generated.

3.2. The Resulted Map of Coseismic Horizontal Ground Displacement

Figure 8 shows the horizontal displacement field obtained from the measurements made from all aerial photos used in this study. Topographic stereoscopic residual is also limited, thanks to the small difference in viewing angles between the preearthquake and postearthquake images [*Ayoub et al*., 2009]. The most striking feature in Figure 8 is the abrupt discontinuity, which precisely matches the ruptures mapped along the CLPF. The only other area with significant surface strain lies parallel to CLPF about 2 km to the east, which coincides with the ALF [*Chen et al*., 2007b].

We have created 50 E-W profiles across the fault zones from north to south in the study fault segment at Tsaotun. Each profile corresponds to a 48 m wide swath (Figure S2). Figure 9 shows the locations of profiles 07, 19, 24, 34, A-A′, B-B′, and C-C′. Figures 10–12 and S2 are the E-W component of horizontal displacements along these profiles. We used these profiles to measure the E-W and N-S offsets across the CLPF and the ALF (Figure 13). Results show an average E-W horizontal shortening of 4.9 ± 0.4 m across CLPF only and a total of 6.1 ± 0.6 m across both CLPF and ALF.

4. Discussion

4.1. Comparison of Coseismic Horizontal Strain and Topography—Implications for the Slip Rate and Earthquake Return Period on the CLPF

We compare long-term deformation, as expressed in the topography, with coseismic deformation along three representative profiles (A-A′, B-B′, and C-C′ in Figure 10). Four discontinuities are observed along profile A-A′ at locations exactly matching the surface ruptures documented during the postearthquake

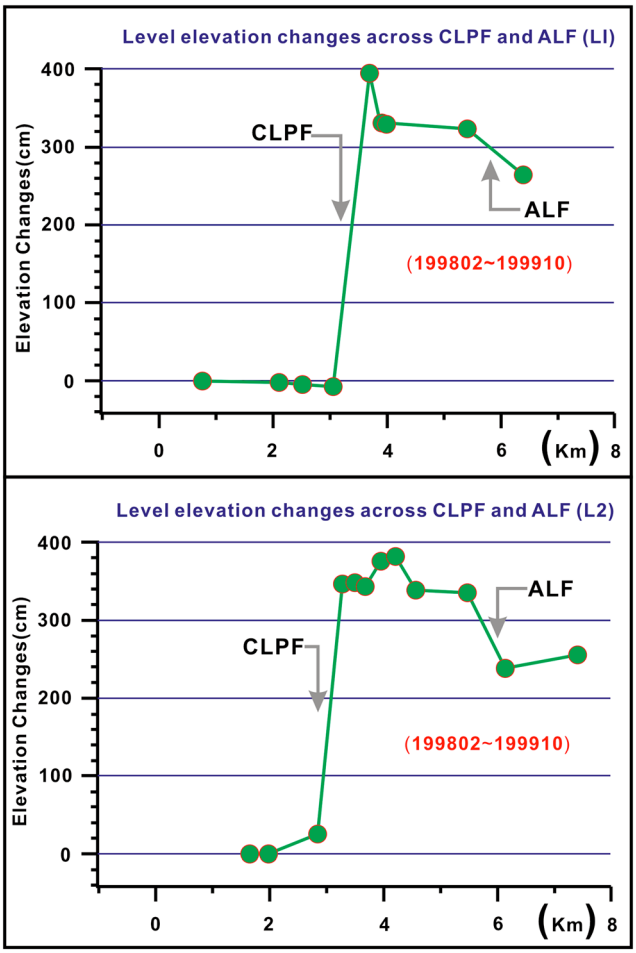

Figure 6. Elevation changes across the Chelungpu fault (CLPF) and the Ailiao fold scarp (ALF) along leveling lines L1 and L2 as determined by comparing field measurements taken before and after the Chi-Chi earthquake in February 1998 and October1999, respectively [after *CGS*, 1999]. See Figure 2 for profile locations.

investigations of Geological Survey of Taiwan [*CGS*, 1999]. The largest step appears at the westernmost location and coincides obviously with the main fault exposure on the ground surface. The other three coincide with minor faults in the hanging wall [*CGS*, 1999]. Profile B-B′ runs through a special location in the township of Tsaotun, where the CLPF branches into two main traces each with similar offsets (2 m). The vertical offset across the easternmost trace is 1.6 m according to the CGS report [*CGS*, 1999], suggesting a dip angle of 39°. Profile C-C′ is the representative of the most common situation where only one major fault trace is observed as a scarp strand. We estimate the fault-perpendicular component of horizontal displacement across CLPF at that location as 4.8 ± 0.4 m, whereas the leveling data [*CGS*, 1999] indicate a vertical component of slip as 3.5 m at the same location (Profile L2 in Figure 6) implying a dip angle of about 36°. All three above profiles show that the horizontal strain across the CLPF correlates remarkably well with the topographic expression manifested in long-term deformation (Figure 10). Coseismic strain as a result of the Chi-Chi earthquake is thus probably representative of the incremental events that have built the topography in the long run.

As we also know, the ratio of the cumulative uplift to coseismic uplift can be used to estimate the amount of fault-perpendicular shortening that must have occurred since the abandonment of the river terraces in Tsaotun area. It is assumed that the fault plane dip angle deduced from coseismic deformation could also be applied to long-term deformation. The close coincidence of coseismic and cumulative deformation pattern supports the assumption that cumulative deformation has resulted from slip along the same fault by many single events as for each provided during the Chi-Chi earthquake. This argument is best supported in profile C-C′ of the area where the main river terrace is not only well preserved in the hanging wall (Figure 2) but is

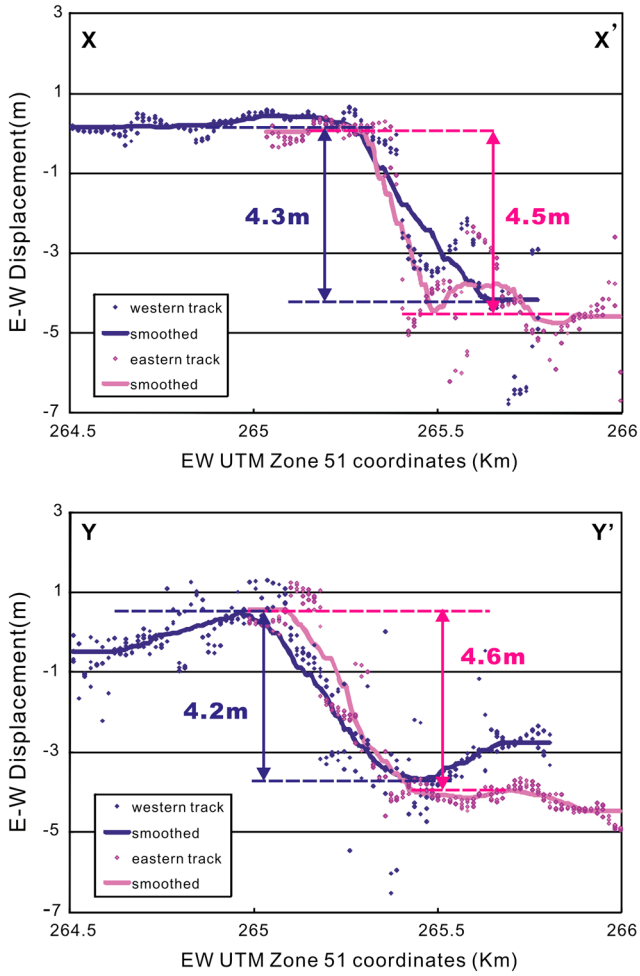

Figure 7. Coseismic east-west horizontal displacements as determined by the east-west disparities measured along X-X′ and Y-Y′ profiles from the correlation of the aerial photos taken along the western (pink) and eastern (blue) tracks. The locations of the X-X′ and Y-Y′ profiles are shown in Figure 3. The apparent offsets across the fault are 4.3 and 4.2 m determined from the western track and 4.5 and 4.6 m from the eastern track, respectively.

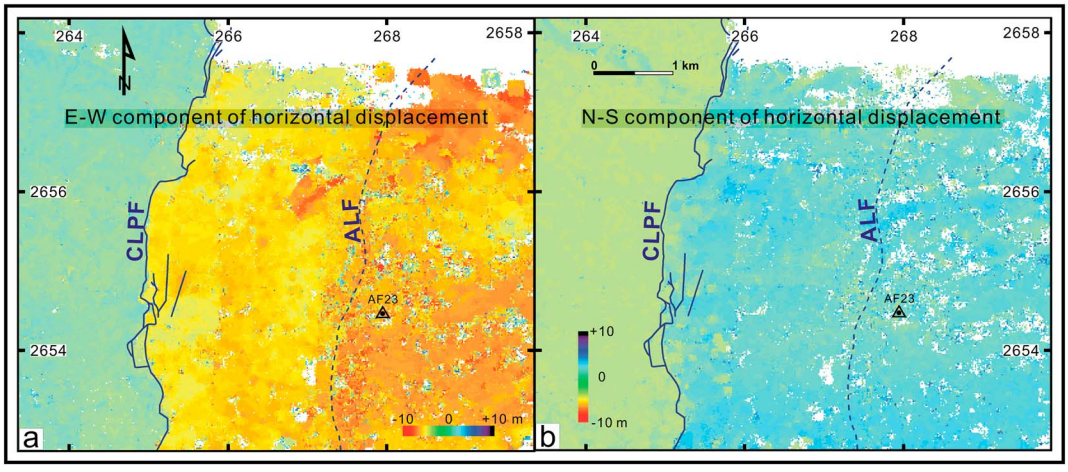

Figure 8. The map of horizontal displacement relative to the footwall measured from the correlation of 12 pairs of aerial photos (Table S1); a correlation window of 128 × 128 m and a sampling of 16 m were used. (a) East-west component and (b) north-south component. The cartographic coordinate system is UTM-51N. The continuous blue line represents the Chi-Chi earthquake surface ruptures along the Chelungpu fault (CLPF) [*CGS*, 1999], and the dashed blue line shows the location of the Ailiao fold scarp (ALF) [*CGS*, 1999; *Chen et al*., 2007a]. The black triangle (AF23) is the location of the Global Positioning System (GPS) data in Tsaotun [*Yu et al*., 2001].

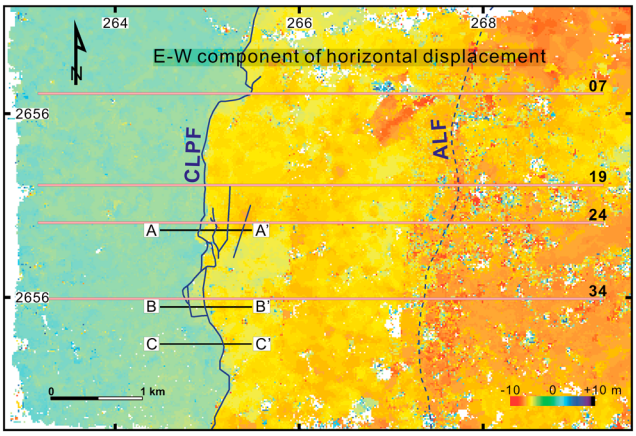

Figure 9. The Chelungpu fault (CLPF) [*CGS*, 1999] is shown as the continuous blue line, and the Ailiao fold scarp (ALF) [*CGS*, 1999; *Chen et al*., 2007a] is shown as the dashed blue line. Locations of profiles (7, 19, 24, and 34) are shown in Figures 11 and 12. Each profile corresponds to a stack within a 48 m wide swath (corresponding to 3 pixels in the disparity map). A-A′, B-B′, and C-C′ show the starting and ending points of the profiles in Figure 10. The coordinate system is UTM-51N.

also dated. The age of river terrace is 11–16 ka according to optically stimulated luminescence (OSL) dating of the sandy layer intercalated within the gravel bed [*Chen et al*., 2003]. The cumulative vertical offset is estimated as 27–34 m, read out from the topographic profile (C-C′). The cumulative uplift is actually larger than the above mentioned reading value, because sedimentation over the footwall needs to be taken into account. A rate of 4.1–6.7 m/kyr has been proposed from a borehole study near Wufeng [*Chen et al*., 2003, 2009]. We therefore estimate the cumulative vertical throw across the CLPF over the last 11–16 ka to be about 45–55 m [*Chen et al*., 2003]. Based on the ratio of vertical and horizontal slip during the Chi-Chi earthquake, we infer that about 101.7 ± 10.1 m of horizontal slip must have accumulated since the abandonment of the river terrace. This implies an average convergence rate of 7.9 ± 2.2 mm/yr across the fault zone over the Holocene and a left-lateral slip rate to 4.5 ± 1.2 mm/yr. The convergence rate is comparable to the 5–8.5 mm/yr estimated from trenching studies that is based on an age coverage of the past 1.9 ka [e.g., *Chen et al*., 2004; *Wang*, 2005] but less than the 12.9 ± 4.8 mm/yr rate estimated from a faulted and folded terrace dated to about 11 ka [*Simoes et al*., 2007]. The difference of the rates may come from the age analysis as our estimate is based on only one age result. Another possibility would be that the short-term rate could be larger than the long-term rate, implying an increasing tectonic rate in the recent past.

Given that recurring earthquakes at one location tend to produce similar slip events [e.g., *Yeats et al*., 1997], we estimate that about 17 events have occurred since the river terrace abandonment. Based on the 11–16 ka OSL age of this terrace, it yields a return period of Chi-chi-like events of about 650–940 yr, which is close to the average recurrence interval of about 700 years for the past 2 ka from trenching studies [*Chen et al*., 2007a].

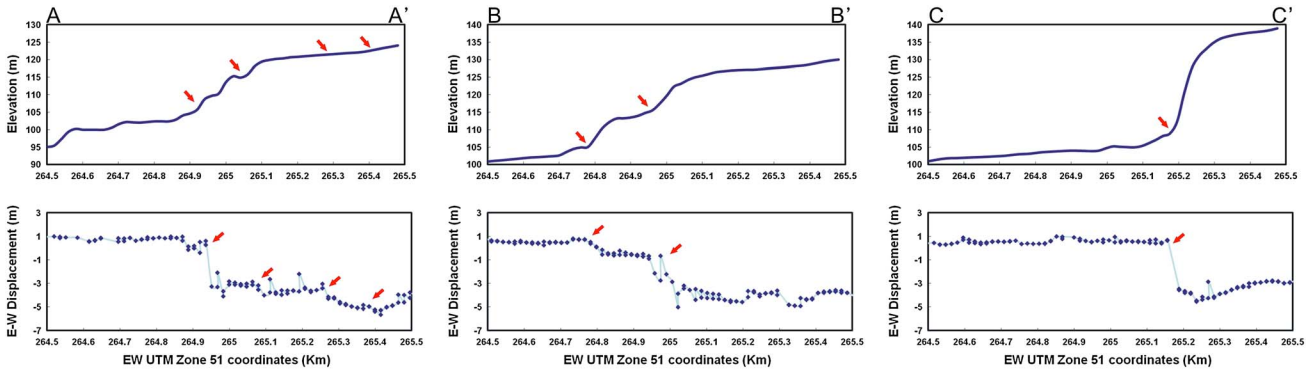

Figure 10. Topography and horizontal east-west surface displacements measured along the profiles A-A′, B-B′, and C-C′. These profiles correspond to close-up views on the Chelungpu fault.

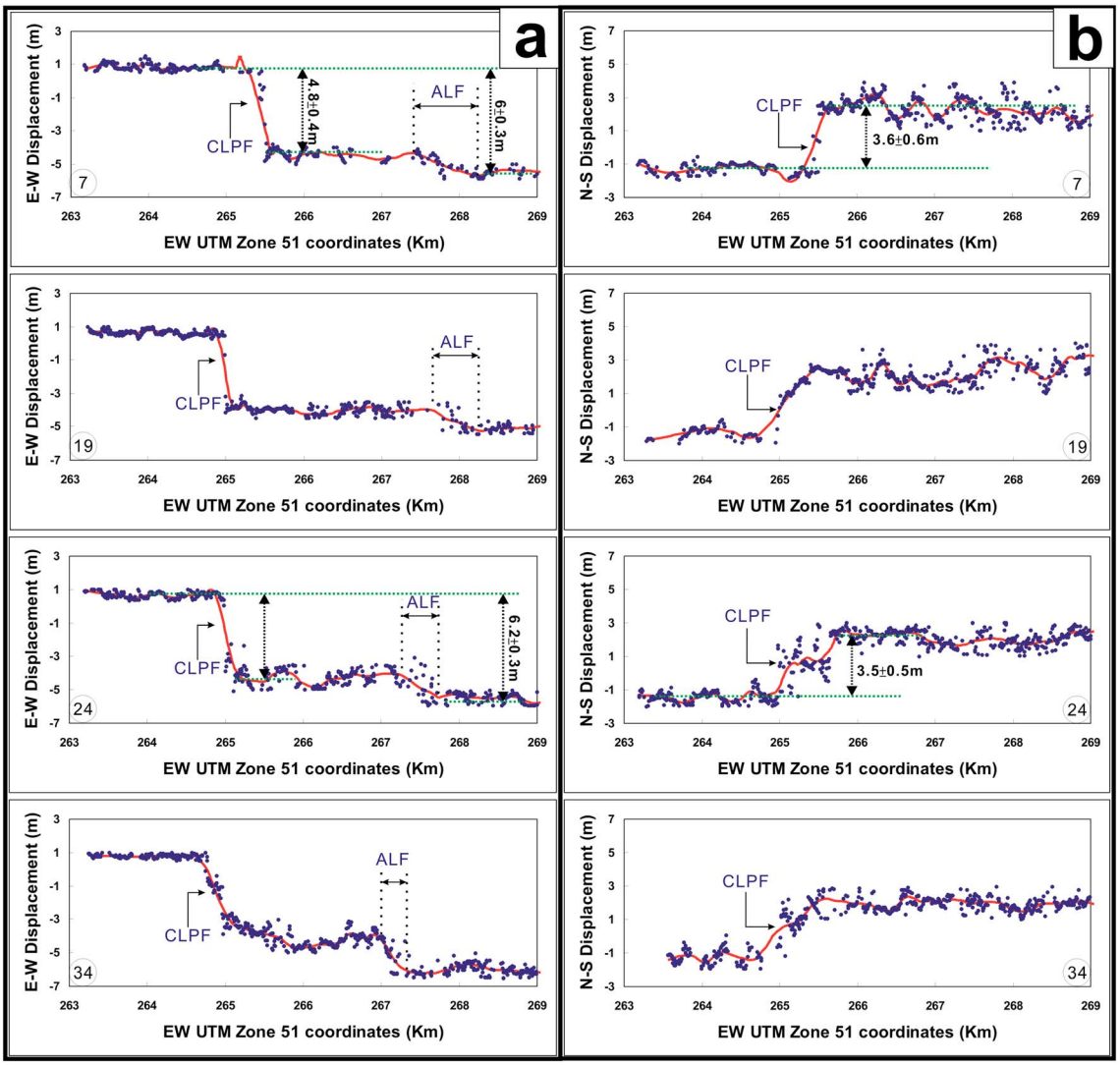

Figure 11. Horizontal (a) east-west and (b) north-south displacements along four selected profiles (7, 19, 24, and 34). The smooth lines in these profiles follow the Negative Exponential Function and use the sampling proportion for 0.1 and polynomial degree for 2. All profiles show a sharp line across the Chelungpu fault (CLPF) and a gradual changing zone of the horizontal displacement across the Ailiao fold scarp (ALF).

4.2. Structural Model of the CLPF From Coseismic Horizontal Ground Displacements

Our measurements show very localized deformation mainly along the CLPF main trace or along the few subsidiary thrust faults that must branch off of the main fault to reach the surface as distinct thrust faults typically within 500 m from the main fault trace (as is seen along profiles A-A′ and B-B′ in Figure 10). The findings is in contrast to the common belief that folding and thrusting must involve some large fraction of off-fault deformation and the fact that distributed deformation has been clearly documented in trenches [*Streig et al*., 2007]. We believe that this distributed deformation reflects tapering of slip on the CLPF because of anelastic deformation of the hanging wall. However, this process occurs only at very shallow depth on the order of a few tens of meters [*Yue et al*., 2005].

We can now use our measurements to infer the CLPF geometry at depth and investigate the relation between the CLPF and the ALF. The fault-perpendicular/fault-parallel components of horizontal displacement across CLPF can be estimated as $4.8 \pm 0.4/3.6 \pm 0.6$ m and $5.1 \pm 0.4/3 \pm 0.4$ m for profiles 7 and 34, respectively (Figures 11 and 12). The vertical uplift across the fault measured at those locations by precise leveling yielded a value to about 3.5 m [*CGS*, 1999] (Figure 6). Based on the above mentioned data, the net slip on the CLPF can be synthesized as about 6.9 m at both locations. Therefore, the dip angle of the shallow portion of the

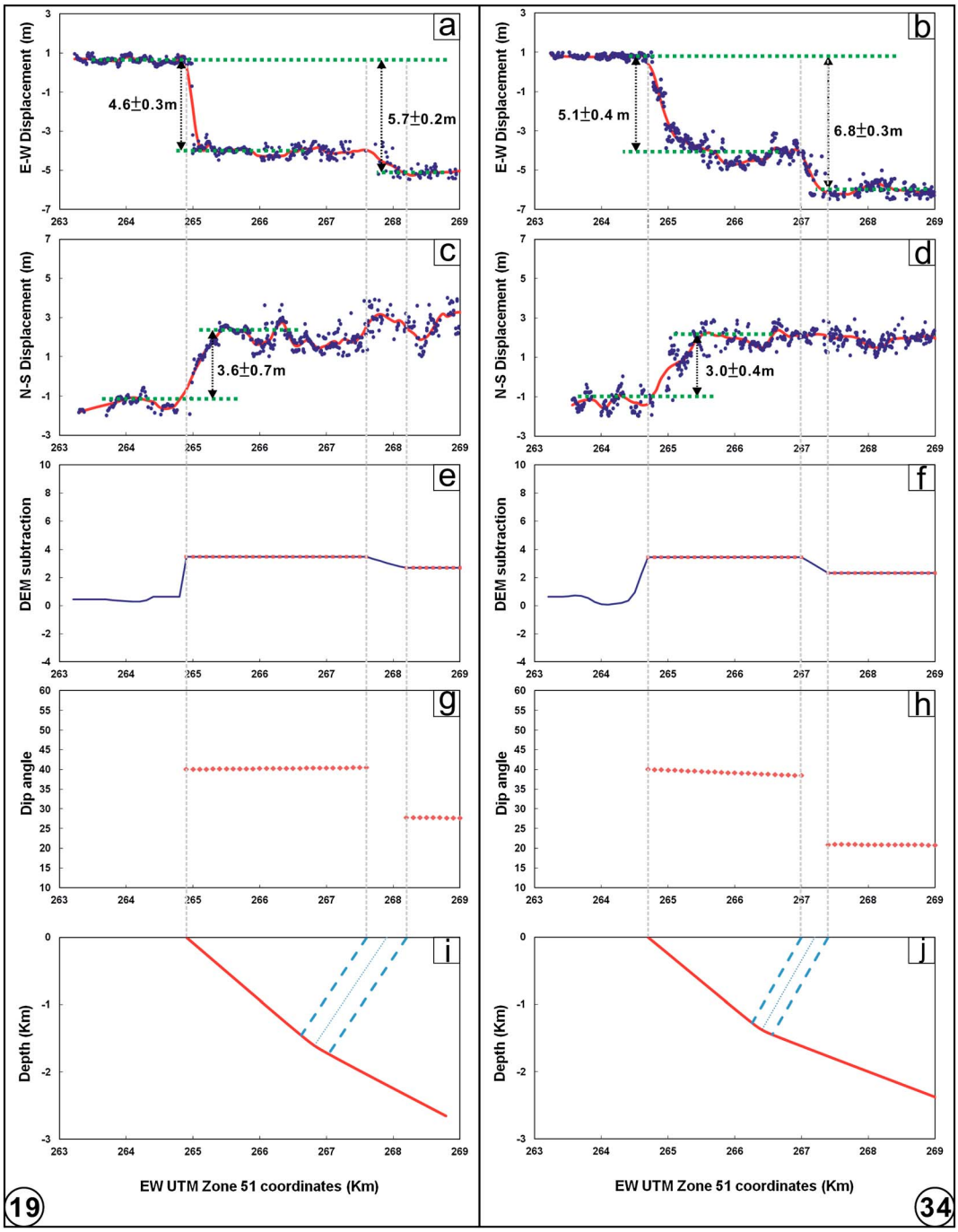

Figure 12. The nineteenth profile, located in the northern study area, yields (a) 4.6 ± 0.3 m and (c) 3.6 ± 0.7 m of horizontal displacements for the E-W and N-S component, respectively, across the Chelungpu fault (CLPF), and the E-W component obviously increases to 5.7 ± 0.2 m (Figure 12a) further across the Ailiao fold scarp (ALF) to the east (Figure 12a). The 34th profile, located in the south, shows (b) 5.1 ± 0.4 and (d) 3.0 ±0.4 m of horizontal displacements for the E-W and N-S component, respectively, across the CLPF, up to 6.8 ± 0.3 for the E-W component eastward across ALF. (e and f) The elevation subtracted preearthquake from postearthquake and the linear regression trend line are respectively shown in blue and red. (g and h) The dip angles calculated by the smooth line of horizontal east-west displacements and the linear regression trend line of elevation subtraction are shown in red. (i and j) The bottom two sketches show simplified fault geometry beneath these two profiles.

CLPF can thus be computed as 36.2 ± 2.2° and 34.5 ± 2.1° along profiles 7 and 34, respectively. However, we note that the leveling data [*CGS*, 1999] (Figure 6) relative to the footwall shows only about 2.6 m of hanging wall uplift more than 2 km to the east of the CLPF, suggesting that the dip angle of the fault might decrease with depth.

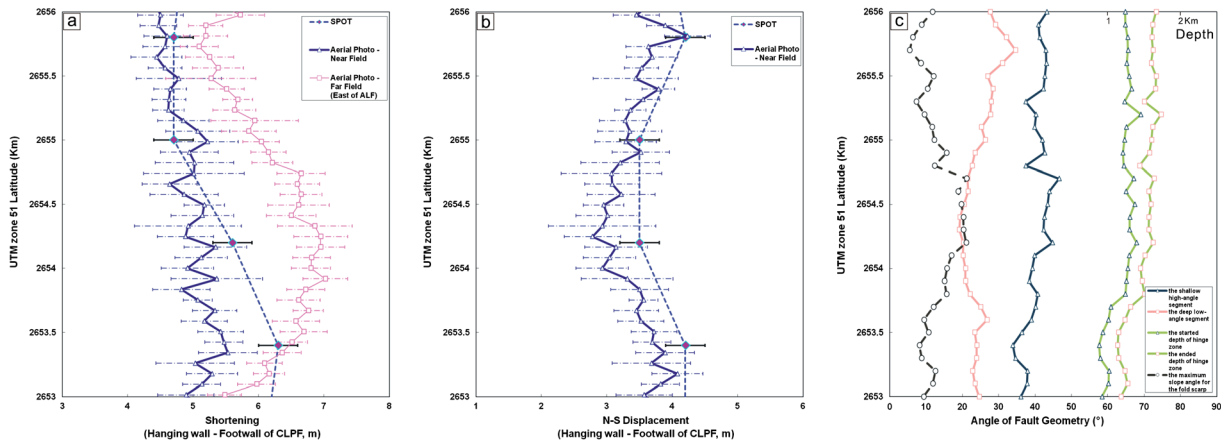

Figure 13. (a) The shortening (~fault perpendicular) and (b) north-south (~fault parallel) components of horizontal surface displacements across the Chelungpu fault (CLPF; blue) and across both the CLPF and the Ailiao fold scarp (ALF; pink) as measured along all of the 50 profiles reported in Figure 8. The measurements of slip on the CLPF made from the correlation of SPOT images [*Dominguez et al*., 2003] are also shown for comparison. (c) The dip angle of fault geometry by shortening and assumed vertical displacement in each profile is shown in blue (shallow high-angle segment) and red (deeper low-angle segment). The beginning and ending depths of hinge zone between these two segments are shown in green.

It has been proposed that the ALF scarp, formerly thought to mark the trace of an active fault called the Ailiao Fault [*Yang*, 1986], would actually be a fold scarp [*Chen et al*., 2007b] (Figure 14). Indeed, field evidence shows that in this area the river terrace was gently tilted forming a monoclinal fold scarp rather than a fault during the Chi-Chi earthquake [*Chen et al*., 2007b]. This interpretation is consistent with our measurements that show a 500–1200 m wide zone of horizontal shortening around the ALF (Figure 11). Furthermore, this monoclinal fold scarp spatially coincides with the surface project of intersection line from a fault bend on the underground CLPF fault plane, which is visible in depths of less than 2 km on seismic profiles [*CGS*, 1999; *Yue et al*., 2005]. The scarp morphology would reflect the finite width of the axial zone formed in association with fault bend and the difference of dip angles between the shallow ramp and the deeper segment [*Chen et al*., 2007b]. By our result, the change of dip angles across that bend can be estimated. As mentioned above, the leveling data [*CGS*, 1999] (Figure 6) show about 2.6 m of uplift for the hanging wall 2 km to the east of CLPF. Our total fault-perpendicular convergence across the ALF and CLPF can be summed up to 6.8 ± 0.3 m

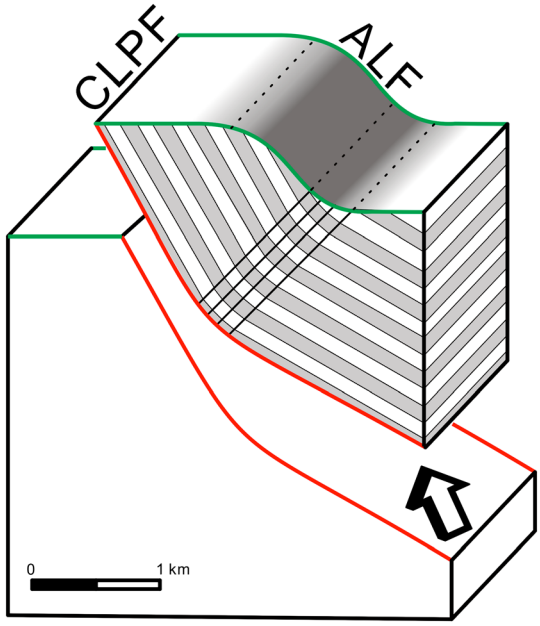

Figure 14. Schematic block diagram showing the fault geometry of the Chelungpu fault and the relationship between fault slip depth and horizontal surface displacements. Seismic profiles [*Yue et al*., 2005] show continuous strata consistent with a fault-bend fold mechanism of folding, as illustrated here. The fold scarp represents the surface expression of the axial hinge zone because of the change of fault dip angle at depth.

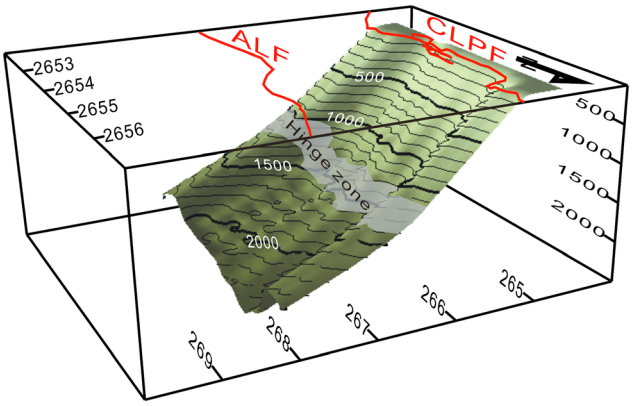

Figure 15. The 3-D view of the fault geometry constructed by steeper upper and gentler lower fault plane as well as a transition hinge zone (in gray). The *XY* coordinate system is UTM-51N.

(Figure 12). This implies a dip angle on the deeper portion of the CLPF of about 20.9 ± 0.8° which is consistent with the seismic profile interpretation of *Yue et al.* [2005]. Our measurements of horizontal contraction across the ALF are quantitatively consistent with its interpretation as a fold scarp manifesting an axial zone associated with a finite-width bend along the CLPF as proposed before [*Chen et al.*, 2007b] (Figure 14).

4.3. Three-Dimensional Fault Geometry Derived by Our Map of Coseismic Ground Displacement

As we learned already from the previously published profile across this region, the CLPF here is characterized by a fault bend located in depth of 1–2 km. However, the detailed 3-D fault geometry can be finally reconstructed when we are able to measure coseismic and high-resolution ground horizontal displacements by COSI-Corr on aerial photos. For this purpose, the vertical displacements are also required to compose the actual ground deformation. We therefore used all the elevation controlling points from the preearthquake and postearthquake 1/5000 Topo-maps to interpolate DEMs in resolution of 100 × 100 m. We then processed subtraction from these two DEMs, thus obtaining the resulting coseismic vertical displacements. For spatial analysis from north to south, 40 E-W profiles of the subtracted DEM are extracted across the fault zones in a resolution of every 100 m. The general pattern for the profiles is similar to that of the horizontal displacement as discussed earlier. Even the variation along the distance is quite high; generally, three segments can be identified as the footwall segment and the two hanging wall segments separated by ALF. After removing the outliers, linear regression trend line for each segment is computed for each profile (e.g., Figure 12). As the coseismic horizontal and vertical displacements have been independently worked out, a composed ground deformation can be further reconstructed for the study area. Based on the composed ground deformation, the fault dips beneath for the profile from north to south (Figure 13c) and the 3-D fault geometry for the CLPF at Tsaotun can be inferred (Figure 15). Our results show that the averaged dip angles are 40.3 ± 3.0° and 24.4 ± 3.6° for the shallow high-angle and deep low-angle fault planes of the CLPF, respectively. However, for the shallow high-angle fault plane, there is a steeper southward trend from 36.6° to 46.6° (2654700, UTM zone 51 latitude) and gentler southward to 33.8° (Figure 13c). On the other hand, the dip angle of the deep low-angle fault plane is 34.6° in the north (2655700, UTM zone 51 latitude) and gradually decreases to a minimum of 19.1° at 2654300 (UTM zone 51 latitude) but increases again southward, which shows a curve in Figure 13c. It is actually a fault bend as shown in Figure 15. The fault bend in the northernmost study area occurs at a depth of 0.9–1.3 km and increases to a depth of 1.5–1.7 km (2655200, UTM zone 51 latitude), and then gradually sinks into 1–1.3 km to the southern boundary of the study area. It is also governed by the zone width of ALF. In addition, at around the location (2654700, UTM zone 51 latitude), the largest dip angle turning across the bend can reach 25.2°, which can produce a maximum slope angle of 21.2° and the average maximum slope angle of 13.0° for the fold scarp on the ALF [*Chen et al.*, 2007b] (Figure 13c).

5. Conclusion

The pattern of coseismic surface deformation caused by the Chi-Chi earthquake in Tsaotun area has been measured with unprecedented accuracy, thanks to the coregistration and correlation of aerial photos using

COSI-Corr. Across the Chelungpu thrust system, the profiles of horizontal displacements demonstrate that the coseismic deformation is either localized in narrow zones of surface faulting (<10 m) or within axial shear zones in the hanging wall related to fault-bends at depth. These observations are consistent with the previous interpretation of the structure as a fault-bend fold; more specifically, the ALF in the study area is a fold scarp formed over an active axial zone beneath. The cumulative horizontal shortening across the CLPF and ALF amounts to 4.9 ± 0.4 and 6.1 ± 0.6 m, respectively, and left-lateral displacement is 3.4 ± 0.4 m. The dip of fault geometry is 33.8°–46.6° and change to 19.1°–34.6° at the 0.9–1.7 km depth. The large change of dip angle is roughly shown at 2654700 (UTM zone 51 latitude) and become smaller to north and south. The study shows that cumulative deformation expressed in the geomorphology of the CLPF in Tsaotun area is proportional to coseismic deformation as a result of the Chi-Chi earthquake. Based on this observation and the age of abandonment of the river terrace, we infer a shortening rate on the CLPF of 7.9 ± 2.2 mm/yr with a left-lateral slip of 4.5 ± 1.2 mm/yr.

From a methodological point of view, the study demonstrates the interest in aerial photos for tectonic geodesy. This approach produces a distributed high-resolution map in a grid of 128 m^2 for horizontal ground displacements covering the entire study area, which has never been achieved for a coseismic thrusting event before. The vertical displacements, also never being developed by this technique before, are proven as derivable if the overlapping pairs are available. The most important advantage is that this method can take into account any distributed deformation that are difficult to measure in the field, especially for those sites away from the rupture zones. Aerial photos are usually available and archived in many countries, which make this technique very much applicable. The abundant and distributed spatial results are extremely valuable to revisit past earthquakes or to study future earthquakes. In addition, aerial photos can be taken for special purposes and are not limited by time and track as satellite images are. This convenience makes our technique relatively also economical and quick when applied on aerial photos.

Acknowledgments

This study was supported by the IES, and NSC under grants 93-2119-M-002-026, 94-2119-M-002-002, and 95-2119-M-002-041, and the Gordon and Betty Moore Foundation through the Tectonics Observatory at Caltech. We thank CGS for the original geodetic and leveling data. We are also grateful for valuable discussions with Y.M. Wu, Y.C. Chan, Y.J. Hsu, S.J. Lee, J.C. Hu, and C.P. Chang. Finally, we are thankful to the suggestions and comments from the Associate Editor, S. Dominguez, J. Hollingsworth, and an anonymous reviewer.

References

Avouac, J. P., P. Tapponnier, M. Bai, H. You, and G. Wang (1993), Active thrusting and folding along the northern Tien-Shan and Late Cenozoic rotation of the Tarim relative to Dzungaria and Kazakhstan, *J. Geophys. Res.*, *98*, 6755–6804.

Ayoub, F., S. Leprince, R. Binet, K. Lewis, O. Aharonson, and J. P. Avouac (2008), Influence of camera distortions on satellite image registration and change detection applications, Proc, IGARSS, Boston, Mass., July 2008.

Ayoub, F., S. Leprince, and J. P. Avouac (2009), Co-registration and correlation of aerial photographs for ground deformation measurements, *ISPRS J. Photogramm. Remote Sens.*, *64*(6), 551–560.

Central Geological Survey (CGS) (1999), Investigation report of 921 earthquake geology and map of surface ruptures along the Chelungpu Fault during the 1999 Chi-Chi earthquake (in Chinese), Minist. of Econ. Affairs, Taipei, Taiwan.

Chen, W. S., K. J. Lee, L. S. Lee, D. J. Ponti, C. Prentice, Y. G. Chen, H. C. Chang, and Y. H. Lee (2004), Paleoseismology of the Chelungpu Fault during the past 1900 years, *Quat. Int.*, *115/116*, 167–176.

Chen, W. S., et al. (2007a), Late Holocene paleoseismicity of the southern part of the Chelungpu fault in central Taiwan: Evidence from the Chushan excavation site, *Bull. Seismol. Soc. Am.*, *97*, 1–13.

Chen, Y. G., W. S. Chen, J. C. Lee, Y. H. Lee, C. T. Lee, H. C. Chang, and C. H. Lo (2001), Surface rupture of 1999 Chi-Chi earthquake yields insights on active tectonics of central Taiwan, *Bull. Seismol. Soc. Am.*, *91*, 977–985.

Chen, Y. G., W. S. Chen, Y. Wang, P. W. Lo, J. C. Lee, and T. K. Liu (2002), Geomorphic evidence for prior earthquakes: Lessons from the 1999 Chichi earthquake in central Taiwan, *Geology*, *30*, 171–174.

Chen, Y. G., Y. W. Chen, W. S. Chen, J. F. Zhang, H. Zhao, L. P. Zhou, and S. H. Li (2003), Preliminary results of long-term slip rates of 1999 earthquake fault by luminescence and radiocarbon dating, *Quat. Sci. Rev.*, *22*, 1213–1221.

Chen, Y. G., K. Y. Lai, Y. H. Lee, J. Suppe, W. S. Chen, Y. N. N. Lin, Y. Wang, J. H. Hung, and Y. T. Kuo (2007b), Coseismic fold scarps and their kinematic behavior in the 1999 Chi-Chi earthquake Taiwan, *J. Geophys. Res.*, *112*, B03S02, doi:10.1029/2006JB004388.

Chen, Y. G., Y. W. Chen, W. S. Chen, K. J. Lee, L. S. Lee, S. T. Lu, Y. H. Lee, T. Watanuki, and Y. N. N. Lin (2009), Optical dating of a sedimentary sequence in a trenching site on the source fault of the 1999 Chi-Chi earthquake, Taiwan, *Quat. Int.*, *199*, 25–33, doi:10.1016/j.quaint.2009.01.001.

Copley, A., J. P. Avouac, J. Hollingsworth, and S. Leprince (2011), The 2001 Mw 7.6 Bhuj earthquake, low fault friction, and the crustal support of plate driving forces in India, *J. Geophys. Res.*, *116*, B08405, doi:10.1029/2010JB008137.

Dolan, J. F., and J. P. Avouac (2007), Introduction to special section: Active fault-related folding: Structural evolution, geomorphologic expression, paleoseismology, and seismic hazards, *J. Geophys. Res.*, *112*, B03S01, doi:10.1029/2007JB004952.

Dominguez, S., J. P. Avouac, and R. Michel (2003), Horizontal coseismic deformation of the 1999 Chi-Chi earthquake measured from SPOT satellite images: Implications for the seismic cycle along the western foothills of central Taiwan, *J. Geophys. Res.*, *108*(B2), 2083, doi:10.1029/2001JB000951.

Gabriel, A. K., R. M. Goldstein, and H. A. Zebker (1989), Mapping small elevation changes over large areas: Differential radar interferometry, *J. Geophys. Res.*, *94*(B7), 9183–9191.

Hollingsworth, J., S. Leprince, F. Ayoub, and J. P. Avouac (2012), Deformation during the 1975–1984 Krafla rifting crisis, NE Iceland, measured from historical optical imagery, *J. Geophys. Res.*, *117*, B11407, doi:10.1029/2012JB009140.

Hollingsworth, J., S. Leprince, F. Ayoub, and J. P. Avouac (2013), New constraints on dike injection and fault slip during the 1975–1984 Krafla rift crisis, NE Iceland, *J. Geophys. Res. Solid Earth*, *118*, 3707–3727, doi:10.1002/jgrb.50223.

Hsu, Y. J., J. P. Avouac, S. B. Yu, C. H. Chang, Y. M. Wu, and J. Woessner (2009), Spatio-temporal slip, and stress level on the faults within the Western Foothills of Taiwan: Implications for fault frictional properties, *Pure Appl. Geophys.*, *166*, 1853–1884.

Ji, C., D. V. Helmberger, T. R. A. Song, K. F. Ma, and D. J. Wald (2001), Slip distribution and tectonic implication of the 1999 Chi-Chi, Taiwan, earthquake, *Geophys. Res. Lett.*, *28*, 4379–4382.
Johnson, K. M., Y. J. Hsu, P. Segall, and S. B. Yu (2001), Fault geometry and slip distribution of the 1999 Chi-Chi, Taiwan earthquake imaged from inversion of GPS data, *Geophys. Res. Lett.*, *28*, 2285–2288.
Kikuchi, M., Y. Yagi, and Y. Yamanaka (2000), Source process of the Chi-Chi Taiwan earthquake of September 21, 1999 inferred from teleseismic body waves, *Bull. Earthquake Res. Inst. Univ. Tokyo*, *75*, 1–13.
Klinger, Y., R. Michel, and G. C. P. King (2006), Evidence for an earthquake barrier model from Mw similar to 7.8 Kokoxili (Tibet) earthquake slip-distribution, *Earth Planet. Sci. Lett.*, *242*, 354–364.
Lee, J. C., Y. G. Chen, K. Sieh, K. Mueller, W. S. Chen, H. T. Chu, Y. C. Chan, C. M. Rubin, and R. Yeats (2001), A vertical exposure of the 1999 surface rupture of the Chelungpu Fault at Wufeng, western Taiwan: Structural and paleoseismic implications for an active thrust fault, *Bull. Seismol. Soc. Am.*, *91*, 914–929.
Leprince, S., S. Barbot, F. Ayoub, and J. P. Avouac (2007), Automatic, precise, ortho-rectification and co-registration for satellite image correlation, application to seismotectonic, *IEEE Trans. Geosci. Remote Sens.*, *45*, 1529–1558.
Loevenbruck, A., R. Cattin, X. Le Pichon, S. Dominguez, and R. Michel (2004), Coseismic slip resolution and post-seismic relaxation time of the 1999 Chi-Chi, Taiwan, earthquake as constrained by geological observations, geodetic measurements and seismicity, *Geophys. J. Int.*, *158*, 310–326.
Ma, K. F., T. R. A. Song, S. J. Lee, and H. I. Wu (2000), Spatial slip distribution of the September 20, 1999, Chi-Chi, Taiwan, earthquake (Mw 7.6)—Inverted from teleseismic data, *Geophys. Res. Lett.*, *27*, 3417–3420.
Massonnet, D., and K. L. Feigl (1998), Radar interferometry and its application to changes in the Earth's surface, *Rev. Geophys.*, *36*(4), 441–500.
Massonnet, D., and T. Rabaute (1993), Radar interferometry: Limits and potential, *IEEE Trans. Geosci. Remote Sens.*, *31*(2), 455–464.
Massonnet, D., M. Rossi, C. Carmona, F. Adragna, G. Peltzer, K. Feigl, and T. Rabaute (1993), The displacement field of the Landers earthquake mapped by radar interferometry, *Nature*, *364*, 138–142.
McGill, S. F., and C. M. Rubin (1999), Surficial slip distribution on the central Emerson fault during the June 28, 1992, Landers earthquake, California, *J. Geophys. Res.*, *104*, 4811–4833.
Michel, R., and J. P. Avouac (2002), Deformation due to the 17 August Izmit earthquake measured from SPOT images, *J. Geophys. Res.*, *107*(B4), 2062, doi:10.1029/2000JB000102.
Michel, R., and J. P. Avouac (2006), Coseismic surface deformation from air photos: The Kickapoo step over in the 1992 Landers rupture, *J. Geophys. Res.*, *111*, B03408, doi:10.1029/2005JB003776.
Murakami, M., M. Tobita, S. Fujiwara, T. Saito, and H. Masaharu (1996), Coseismic crustal deformations of 1994 Northridge, California, earthquake detected by interferometric JERS 1 synthetic aperture radar, *J. Geophys. Res.*, *101*(B4), 8605–8614.
Rockwell, T. K., S. Lindvall, T. Dawson, R. Langridge, W. Lettis, and Y. Klinger (2002), Lateral offsets on surveyed cultural features resulting from the 1999 Izmit and Duzce Earthquakes, Turkey, *Bull. Seismol. Soc. Am.*, *92*, 79–94, doi:10.1785/0120000809.
Roering, J. J., M. L. Cooke, and D. D. Pollard (1997), Why blind thrust faults don't propagate to the Earth's surface: Numerical modeling of coseismic deformation associated with thrust-related anticlines, *J. Geophys. Res.*, *102*, 11,901–11,912.
Simoes, M., J. P. Avouac, and Y. G. Chen (2007), Slip rates on the Chelungpu and Chushiang thrust faults inferred from a deformed strath terrace along the Dungpuna river, west central Taiwan, *J. Geophys. Res.*, *112*, B03S10, doi:10.1029/2005JB004200.
Streig, A. R., C. M. Rubin, W. S. Chen, Y. G. Chen, L. S. Lee, S. C. Thompson, C. Madden, and S. T. Lu (2007), Evidence for prehistoric coseismic folding along the Tsaotun segment of the Chelungpu fault near Nan-Tou, Taiwan, *J. Geophys. Res.*, *112*, B03S06, doi:10.1029/2006JB004493.
Van Puymbroeck, N., R. Michel, R. Binet, J. P. Avouac, and J. Taboury (2000), Measuring earthquakes from optical satellite images, *Appl. Optics Inf. Process.*, *39*(23), 3486–3494.
Wang, J. H. (2005), Earthquakes rupturing the Chelungpu fault in Taiwan are time predictable, *Geophys. Res. Lett.*, *32*, L06316, doi:10.1029/2004GL021884.
Wu, F. T. (1978), Recent tectonics of Taiwan, *J. Phys. Earth*, *26*, 265–299 Suppl.
Yang, G. S. (1986), A geomorphological study of active faults in Taiwan—Especially on the relation between active faults and geomorphic surfaces (in Chinese), Ph.D. thesis, 178pp, Chinese Culture University, Taipei, Taiwan.
Yeats, R. S., K. Sieh, and C. R. Allen (1997), *The Geology of Earthquakes*, pp. 568, Oxford Univ. Press, New York.
Yu, S. B., H. Y. Chen, and L. C. Kuo (1997), Velocity field of GPS stations in the Taiwan area, *Tectonophysics*, *274*, 41–59.
Yu, S. B., et al. (2001), Preseismic deformation and coseismic displacements associated with the 1999 Chi-Chi, Taiwan earthquake, *Bull. Seismol. Soc. Am.*, *91*, 995–1012.
Yue, L. F., J. Suppe, and J. H. Hung (2005), Structural geology of a classic thrust belt earthquake: The 1999 Chi-Chi earthquake Taiwan (Mw = 7.6), *J. Struct. Geology*, *27*, 2058–2083.
Zebker, H. A., P. A. Rosen, R. M. Goldstein, A. Gabriel, and C. L. Werner (1994), On the derivation of coseismic displacement field using differential Radar interferometry: The Landers earthquake, *J. Geophys. Res.*, *99*(B10), 19,617–19,634.